NANO LETTERS
Cite This: Nano Lett. XXXX, XXX, XXX−XXX
Letter
pubs.acs.org/NanoLett

Tunable Infrared Metasurface on a Soft Polymer Scaffold

Jeremy B. Reeves,[*,†] Rachael K. Jayne,[‡] Thomas J. Stark,[¶] Lawrence K. Barrett,[¶] Alice E. White,[‡,¶,§] and David J. Bishop[†,‡,¶,§]

[†]Department of Electrical and Computer Engineering, Boston University, Boston, Massachusetts 02215, United States
[‡]Department of Mechanical Engineering, Boston University, Boston, Massachusetts 02215, United States
[¶]Division of Materials Science and Engineering, Boston University, Boston, Massachusetts 02215, United States
[§]Department of Physics, Boston University, Boston, Massachusetts 02215, United States

ABSTRACT: The fabrication of metallic electromagnetic meta-atoms on a soft microstructured polymer scaffold using a MEMS-based stencil lithography technique is demonstrated. Using this technique, complex metasurfaces that are generally impossible to fabricate with traditional photolithographic techniques are created. By engineering the mechanical deformation of the polymer scaffold, the metasurface reflectivity in the mid-infrared can be tuned by the application of moderate strains.

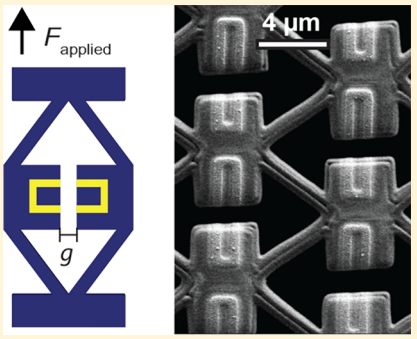

KEYWORDS: *microelectromechanical systems (MEMS), stencil lithography, direct laser writing, metasurface, metamaterial*

Metasurfaces are two-dimensional electromagnetic materials with properties determined by the geometry of subwavelength structures, or meta-atoms, rather than the bulk material properties. Recently, metasurfaces have begun to achieve the promise of flat optical elements with versatile capabilities, including beam shaping and deflection, switching, hologram formation, and perfect absorption.[1−5] Such devices have exploited a wide range of material platforms.[6,7] Extending the material platforms available for the creation of metasurfaces will continue to enhance metasurface functionality.

Metasurfaces relying on subwavelength metallic or dielectric resonators have properties fixed by the meta-atom geometry, limiting these devices to operation in a narrow spectral band. Some work has extended the operating bandwidth through increased design complexity and more complicated meta-atom geometries;[8,9] applications such as tunable filters or sensors require dynamically reconfigurable metasurfaces. Dynamic control of optical properties has been achieved through the implementation of phase change materials,[10] liquid crystals,[11] and optically excited carriers.[12] Mechanical tuning through microelectromechanical systems (MEMS),[13−15] flexible substrates,[16,17] or optical forces[18] also provides routes to realizing dynamic electromagnetic metasurfaces by manipulating the meta-atom geometry.

Mechanical control of otherwise static materials has enabled frequency-agile devices[19] by taking advantage of the interactions between meta-atoms in the near-field[14,20] or changes in spatial orientation of the meta-atoms.[15] As illustrated in Figure 1a,b, metasurfaces with unit cells consisting of closely spaced resonant elements are tunable through control of near-field interactions between the elements. Here, small changes to the spacing g of an asymmetric split ring resonator (ASRR) provide tunability. By controlling g, frequency tunable metasurfaces on stretchable substrates have been used to demonstrate continuous tuning of reflection peaks,[17] which has utility for strain sensors[21] and biochemical applications.[22,23]

The design of mechanically tunable metasurfaces must account for unwanted side effects, such as permanent deformation of the meta-atoms and delamination, associated with the deformation of the substrate. Such effects irreversibly change the design response of the metasurface and limit the surface's lifetime in a dynamic environment. In addition, distortion of the meta-atoms can lead to effects that reduce the overall tunability of the device.[17] The deformation of the substrate requires consideration when designing the metasurface pattern.[24] Furthermore, the materials available for these types of metasurfaces are also limited, as many are incompatible with solvents and ultraviolet or electron beam exposure used in typical planar lithographic techniques.

In this letter, a method for the fabrication of geometrically tunable optical metasurfaces based on 3D soft mechanically engineered scaffolds is described. Patterning mechanical metamaterial scaffolds with optical meta-atoms enables a new class of metasurfaces with enhanced control over the mechanical deformation. The scaffold's underlying geometry is leveraged to design the deformation of individual meta-atoms comprising the optical unit cells and to define the scaffold's

Received: November 29, 2017
Revised: April 4, 2018

DOI: 10.1021/acs.nanolett.7b05042
Nano Lett. XXXX, XXX, XXX−XXX

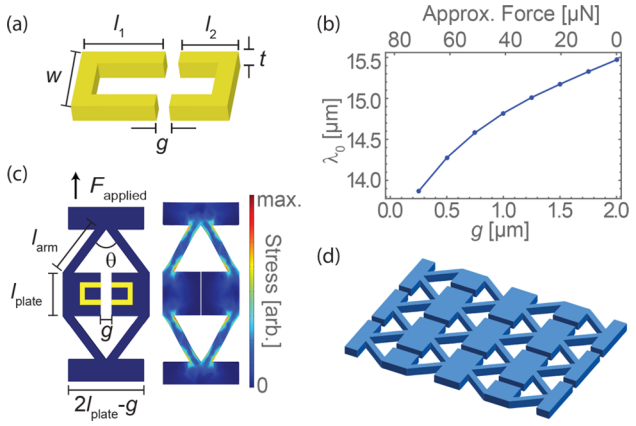

Figure 1. Mechanical metamaterials combined with optical meta-atoms to produce tunable metasurfaces. (a) Schematic of the asymmetric split ring resonator, parametrized by arm lengths l_1 and l_2, width w, thickness t, and gap spacing g. (b) Resonant wavelength λ_0, calculated from numerical finite-difference time-domain reflection data, of the magnetic mode of the asymmetric split ring resonator in the case of $l_1 = l_2 = 2.4$ μm. The force required to adjust g for a 10 by 10 array of the unit cells in (c) is also plotted along the horizontal axis. (c) Left: An unstrained unit cell of a mechanical scaffold capable of tuning g with the application of a uniaxial force $F_{applied}$. When strain is applied, the unit cell stretches as on the right, reducing g. The stress experienced by the strained unit cell is encoded in its coloring. (d) Array of unit cells that make up the mechanical scaffold.

overall mechanical properties. As illustrated in Figure 1c,d, a honeycomb structure can be used to control the separation of closely spaced elements. When strained, the metasurface unit cells deform uniaxially without straining the metallic pattern deposited on the surface. Figure 1c shows the stress pattern and deformation mode of the unit cell as calculated using COMSOL for typical polymer material constants, locations of high stress are localized near the joints of the arms and plates. The forces required to achieve the strains required to close the gap are also estimated and correlated with the gap size in Figure 1b.

For the experiments described here, we use unit cell design parameters $l_{arm} = 5$ μm, $l_{plate} = 4$ μm, $\theta = 74°$, and $g = 1$ μm with a thickness of 2 μm. These parameters yield a scaffold with a Poisson's ratio of $\nu = 1.45$, which is large compared to typical stretchable substrates like PDMS with $\nu \approx 0.5$. The large engineered ν enhances the meta-atom displacement for relatively small strains without deformation of the meta-atom shape as the strain is localized in the scaffold arms. A compromise between the length, angle, and width of the arms is required, such that the scaffold deforms primarily by bending at the joints between the arms and the plates, as in Figure 1, while being thick enough to avoid collapsing under its own weight. In order to minimize the unit cell's size, we define the arms using two passes of the DLW laser focus, yielding a height to width ratio of ~1.5 and a scaffold that is mechanically supported. The length and angle are then selected to ensure the two halves of each meta-atom experience a large displacement with small strains. It should be noted that, while an unconstrained sheet composed of these unit cells will compress uniformly in the direction orthogonal to the strain, we are limited to scaffolds anchored at either end. The boundary conditions imposed by anchoring lead to a distribution of unit cell deformations across the scaffold, which in turn leads to a distribution of meta-atom gap sizes.

Arbitrary flexible and freestanding 3D mechanical metamaterial scaffolds are produced using direct laser writing (DLW), which is an advanced 3D fabrication technique based on two-photon polymerization.[25,26] To fabricate the 3D structures, we use a commercial DLW system (Nanoscribe Photonic Professional GT) equipped with a 63× oil immersion objective lens with NA = 1.4 to achieve a lateral writing resolution of ~0.2 μm and vertical resolution of 0.6 μm. These structures can be fabricated in roughly 60 s in a variety of photoresists, with properties selected for the specific application. Fabrication of anchors and supports accounts for most of the print time while the scaffold lattice itself is printed in about 5 s. We use the proprietary resist IP-Dip (Nanoscribe). The overall size of the scaffold is presently limited by the writing area of the commercial DLW system; larger scaffolds can be fabricated, but would require stitching patterns together resulting in small pattern misalignments and mechanically weak seams. In order to print meta-atom arrays on the DLW-scaffolds, we rely on stencil masks to eliminate the need for photoresists and other processing steps incompatible with the delicate structures.

Our technique, based on atomic calligraphy,[27,28] relies on MEMS stencil masks to precisely pattern the DLW-produced scaffolds. The MEMS devices are fabricated by the MEMSCAP multiuser foundry using the polyMUMPS process.[29] The foundry process produces one fixed and two movable mechanical layers, denoted P1 (bottom) and P2 (top), of polycrystalline silicon with a minimum features size of 2 μm. The device, described in Figure 2, features P2 plates tethered to

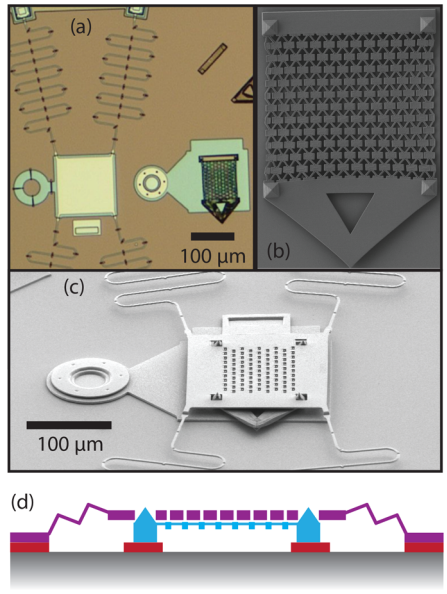

Figure 2. Devices and methods for the fabrication of electromagnetic metasurface on a polymer scaffold. (a) Optical image of a representative device showing mask, spring tethers and polymer scaffold. (b) SEM micrograph of the 2D metamaterial scaffold. A floating triangular handle (bottom) is fabricated opposite the anchored end of the scaffold (top), allowing for mechanical manipulation. (c) SEM micrograph of the device in (a) after FIB milling of the mask and positioning of the scaffold. (d) Schematic cross section of a MEMS mask device. The MEMS substrate, P1, and P2 layers are gray, red, and purple, respectively. The DLW polymer scaffold is blue. Square-pyramid shaped alignment posts align the FIB-milled mask with the structure of the scaffold.

DOI: 10.1021/acs.nanolett.7b05042
Nano Lett. XXXX, XXX, XXX−XXX

the MEMS substrate by flexible serpentine springs in P2 and rotating P1 shuttles. As shown in Figure 2, the DLW process allows for microstructured polymer scaffolds to be printed directly on the MEMS device and the shuttle allows for easy positioning of the scaffold beneath the P2 plate, a process taking just a few minutes.

To align and transfer the mask pattern to the polymer, focused-ion-beam (FIB) milling is used to pattern the P2 plate with a stencil mask having features as small as 10 nm. Alignment holes, milled to closely match the shape of the DLW-printed alignment pillars, are also milled through the plate. In tandem with alignment pillars attached to the DLW-printed scaffold, the alignment holes allow for micron-level pin alignment and help to secure the mask-scaffold sample during alignment and physical vapor deposition (PVD); see Figure 2c. The alignment pillars stand taller than the P2 plate and encourage a "snapping" of the mask into alignment with the scaffold while ensuring secure contact between mask and scaffold. The spring tethers are pliant enough to accommodate any small misalignment of the mask and scaffold positions, as in Figure 2c,d. Once interlocked with the alignment pillars, the springs are stiff enough to hold the assembled mask-scaffold structure securely in place during subsequent manipulation and PVD. The PVD step takes about 2 h, limited by the time required to transfer samples to high vacuum.

With the mask in place, aluminum meta-atoms are deposited on the polymer scaffold using a Meivac electron beam evaporator with deposition rates of 3–5 Å/s at pressures below 6×10^{-6} Torr. After deposition of the meta-atom pattern, the mask is removed and the metal-patterned polymer is suspended above holes on a sacrificial substrate, in order to prevent optical interference due to back-reflections from the MEMS substrate.

We choose the ASRR unit cell for its broad tunability stemming from a tunable hybridization of the individual split ring resonances, which can be controlled via the gap g between split rings. Furthermore, the resonance can be positioned in the mid-infrared by scaling the geometry appropriately. Split ring parameters $l_1 = 2.8$ μm, $l_2 = 1.5$ μm, $w = 1.5$ μm, with $t \approx 100$ nm and wire width ≈ 0.6 μm and an initial gap of $g = 1$ μm are selected to produce resonances in a region of high photon flux for typical thermal radiation sources. An electron micrograph of a representative device is shown in Figure 3a. The relative alignment between the polymer scaffold and the PVD metallic pattern is accurate to better than 0.5 μm across the entire device.

Spectroscopic measurements are performed using a Fourier-transform infrared (FTIR) spectrometer (Bruker Vertex 70V). An attached microscope (Bruker Hyperion 1000) in reflection mode with Cassegrain optics, including a 20×, NA = 0.6 objective (Bruker) and a knife-edge aperture in the conjugate image plane, allows for collection of light from regions smaller than 100×100 μm^2. Here, we collect light from the central 100 unit cells of the metasurface. All spectral measurements are performed in dry air and referenced to a standard gold mirror. The polymer scaffold, prior to patterning, has an average intensity reflection coefficient $R \approx 0.05$ and is consistent with measurements of the IP-Dip refractive index of $n = 1.53$.[30] The bare scaffold reflectivity is the dotted black line in Figure 3b. There is no significant change in the bare scaffold reflectivity with respect to polarization, the plotted line represents the mean of spectra with polarizations along the long and short axis of the unit cell.

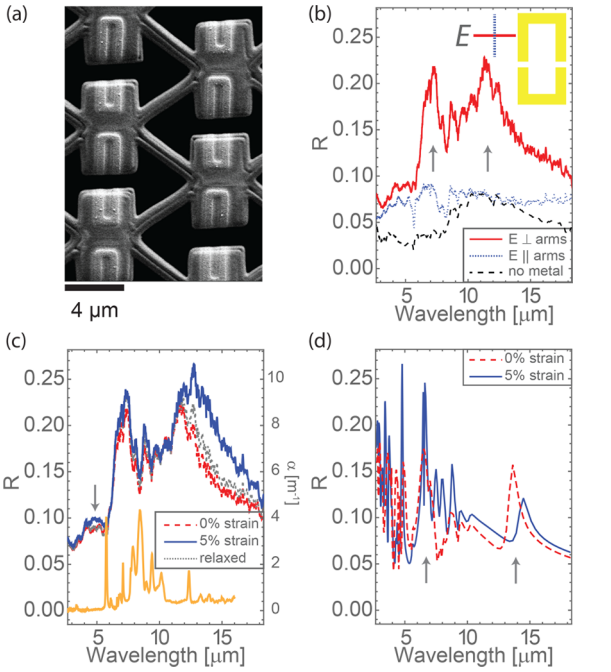

Figure 3. Metasurface and infrared reflectivity data. (a) Electron micrograph of the composite scaffold showing good alignment between the metallic layer and the underlying scaffold. Evidence of small misalignments due to a rotation of the mask with respect to the scaffold and imperfections in the scaffold structure are just visible. (b) Reflection spectra of the metal patterned scaffold for orthogonal polarizations in solid red (perpendicular to the arms) and dotted blue (along the arms). The reflectivity data averaged over both polarizations for the scaffold prior to metal patterning is plotted in dashed black. Arrows indicate the location of the ASRR resonance peaks. (c) For light polarized perpendicular to the arms, the reflection spectra of the patterned scaffold before, during, and after 5% strain are plotted in dashed red, solid blue, and dotted gray, respectively. The absorption coefficient α of IP-Dip is plotted in orange for comparison. The arrow highlights a reflectivity enhancement at short wavelengths for the strained sample. (d) FDTD results for a simulated system accounting for the scaffold geometry and polymer optical properties; the strained (dashed red) and unstrained (solid blue) reflectance spectra are plotted. Arrows indicate the location of the ASRR resonance peaks.

When patterned with ASRRs, the reflection spectrum becomes strongly polarization dependent. Spectra for orthogonal polarizations, aligned along and perpendicular to the ASRR arms, are plotted in Figure 3b. When polarized along the arms, as plotted in blue, the reflectivity is enhanced slightly. Narrow absorption features characteristic of IP-Dip, seen as reflectivity dips at 5.75 and 8 μm, are enhanced due to the large fields associated with the metallic patterning. When the incident electric field is polarized perpendicular to the ASRR arms, two peaks at about 7 and 11.5 μm associated with the magnetic resonances of the individual split rings are observed.

We strain the metasurfaces by pulling on the DLW-printed handle using a micromanipulator with positioning resolution better than 0.5 μm. Under applied strain, the gap in the ASRRs is closed as described in Figure 1c, and a red-shift of about 1 μm is observed in the long wavelength peak, as seen in Figure 3c. This shift is accompanied by significant broadening of the resonance line. The peak locations are determined by fitting the peaks with an asymmetric Gaussian line shape to account for a distribution of ASRR arm lengths due to small (<0.5 μm) misalignments across the scaffold. The maximum strain applied,

DOI: 10.1021/acs.nanolett.7b05042
Nano Lett. XXXX, XXX, XXX−XXX

measured using an optical microscope, is ~5%. A significant change in the reflection spectrum is observed for small strains, enabled by the microstructured geometry of the underlying scaffold. After the strain is released, the spectrum nearly returns to the initial state, as shown by the dotted gray line in Figure 3c. While the polymerized resist is viscoelastic and some plastic deformation is to be expected at the joints, we estimate this effect to be small. The scaffold allows for the use of smaller strains to achieve displacements, which would require much larger strains (10% or more) on bulk elastic substrates.[16,17] Furthermore, since the deformations result from bending in the arms, rather than stretching, the substrate material around the meta-atoms is not deformed, and stresses in the substrate and pattern material can be kept to a minimum.

The resonance shift is estimated using commercial finite-difference time-domain (FDTD) simulations (Lumerical-FDTD Solutions) of Al ASRR arrays, with dimensions matching the experimental design as in Figure 3d. The simulations assume an infinite array of ideally deforming scaffold unit cells patterned with ASRR elements. To account for the optical properties of the polymerized IP-Dip, we measure the imaginary part of the substrate refractive index $\tilde{n} = n + i\kappa$ using FTIR absorption spectroscopy of a 1.7 μm thick IP-Dip film suspended in air. The real part n is calculated using the Kramers–Kronig relationship. The measured absorption coefficient $\alpha = 4\pi\kappa/\lambda$ is plotted in Figure 3c. To model the applied force, we assume the scaffold arms are rigid and bend at their joints to close the gap g within the ASRR. In this way, a 5% strain generates a 1 μm reduction of g. The FDTD model captures the direction and approximate magnitude of the shift of the long wavelength resonance peak. As seen in Figure 3d, a red shift in the long wavelength resonance peak is observed when g is reduced by the application of strain. Broadening of the experimental resonance widths compared to the FDTD resonance widths can be accounted for by additional losses in the granular Al PVD film and a distribution of ASRR parameters due to small misalignments. Using FDTD simulations, we estimate that these effects dominate over any broadening introduced by the distribution of wave-vectors associated with the high NA objective.

While a corresponding blue shift of the short wavelength peak at 7 μm is expected for increased resonator coupling with reduced g, absence of such a shift is readily explained by examining the absorption spectrum of IP-Dip. Strong absorption features in the polymerized resist are visible in the region from 5.5 μm to about 10 μm. These absorption features effectively clip the short wavelength resonance peak, obscuring the expected shift as can be elucidated in Figure 3c. In fact, close inspection reveals a reversible increase in reflectance around 5 μm, which suggests that this shift is obscured by the strong absorption feature at 5.75 μm. Results from the FDTD simulations in Figure 3d corroborate this effect.

The broadening of the resonance peaks with strain in the experimental measurements can be accounted for by a distribution of g arising from the nonuniform deformation of the constrained scaffold. For computation, this effect is not included in the code as the simulations would become prohibitively large. We also note that the many sharp features appearing in the FDTD simulations at wavelengths below 5 μm can be associated with Mie-type resonances in the geometry of the scaffold. These do not appear in the experiment because the DLW-printed scaffold is not composed of an ideal array of uniform rectangular prisms, as is modeled by FDTD.

We have demonstrated, for the first time, a general method for the fabrication of microstructured polymer scaffolds with precise metallic patterning. Our versatile technique has been applied in the fabrication of a metasurface with a tunable reflection spectrum, fabricated on a soft, deformable scaffold. The methods used to fabricate this device can be applied to fully three-dimensional structures and other nonplanar substrates. An iterative process can be used to sandwich metallic and polymer layers, yielding 3D structures that can be usefully patterned with metallic wires or other functionalization using PVD-compatible materials. Beyond these stand-alone devices, integration with MEMS actuators can lead to novel optical MEMS or NEMS with dynamic properties.[31] The generality of the methods presented here open up the possibility of integrating electronics on micron-scale 3D printed sensors and actuators and can even be applied for selective chemical patterning in biomedical applications.

AUTHOR INFORMATION

Corresponding Author

*E-mail: jbr2@bu.edu.

ORCID

Jeremy B. Reeves: 0000-0002-6264-8481

Notes

The authors declare no competing financial interest.

ACKNOWLEDGMENTS

This work was funded by Boston University Photonics Center, Boston University College of Engineering, by the DARPA Atoms to Product (A2P) Program/Air Force Research Laboratory (AFRL) contract no. FA8650-15-C-7545, and by the NSF CELL-MET ERC award no. 1647837. R.K.J. was supported with a Fellowship from the Clare Booth Luce Foundation.

REFERENCES

(1) Zheludev, N. I.; Kivshar, Y. S. *Nat. Mater.* **2012**, *11*, 917–924.
(2) Yu, N.; Capasso, F. *Nat. Mater.* **2014**, *13*, 139–150.
(3) Shalaev, M. I.; Sun, J.; Tsukernik, A.; Pandey, A.; Nikolskiy, K.; Litchinitser, N. M. *Nano Lett.* **2015**, *15*, 6261–6266.
(4) Larouche, S.; Tsai, Y.-J.; Tyler, T.; Jokerst, N. M.; Smith, D. R. *Nat. Mater.* **2012**, *11*, 450–454.
(5) Watts, C. M.; Liu, X.; Padilla, W. J. *Adv. Mater.* **2012**, *24*, OP98–OP120.
(6) Chen, H.-T.; Taylor, A. J.; Yu, N. *Rep. Prog. Phys.* **2016**, *79*, 076401.
(7) Genevet, P.; Capasso, F.; Aieta, F.; Khorasaninejad, M. *Optica* **2017**, *4*, 139–152.
(8) Khorasaninejad, M.; Shi, Z.; Zhu, A. Y.; Chen, W. T.; Sanjeev, V.; Zaidi, A.; Capasso, F. *Nano Lett.* **2017**, *17*, 1819–1824.
(9) Feng, Q.; Pu, M.; Hu, C.; Luo, X. *Opt. Lett.* **2012**, *37*, 2133.
(10) Samson, Z.; MacDonald, K. *Appl. Phys. Lett.* **2010**, *96*, 143105.
(11) Komar, A.; Fang, Z.; Bohn, J.; Sautter, J.; Decker, M.; Miroshnichenko, A.; Pertsch, T.; Brener, I.; Kivshar, Y. S.; Staude, I.; Neshev, D. N. *Appl. Phys. Lett.* **2017**, *110*, 071109.
(12) Chen, H.-T.; O'Hara, J. F.; Azad, A. K.; Taylor, A. J.; Averitt, R. D.; Shrekenhamer, D. B.; Padilla, W. J. *Nat. Photonics* **2008**, *2*, 295–298.
(13) Liu, X.; Padilla, W. J. *Adv. Opt. Mater.* **2013**, *1*, 559–562.
(14) Fu, Y. H.; Liu, A. Q.; Zhu, W. M.; Zhang, X. M.; Tsai, D. P.; Zhang, J. B.; Mei, T.; Tao, J. F.; Guo, H. C.; Zhang, X. H.; Teng, J. H.; Zheludev, N. I.; Lo, G. Q.; Kwong, D. L. *Adv. Funct. Mater.* **2011**, *21*, 3589–3594.
(15) Hu, F.; Qian, Y.; Li, Z.; Niu, J.; Nie, K.; Xiong, X.; Zhang, W.; Peng, Z. *J. Opt.* **2013**, *15*, 055101.

DOI: 10.1021/acs.nanolett.7b05042
Nano Lett. XXXX, XXX, XXX–XXX

(16) Aksu, S.; Huang, M.; Artar, A.; Yanik, A. A.; Selvarasah, S.; Dokmeci, M. R.; Altug, H. *Adv. Mater.* **2011**, *23*, 4422−4430.
(17) Pryce, I. M.; Aydin, K.; Kelaita, Y. A.; Briggs, R. M.; Atwater, H. A. *Nano Lett.* **2010**, *10*, 4222−4227.
(18) Zheludev, N. I.; Plum, E. *Nat. Nanotechnol.* **2016**, *11*, 16−22.
(19) Hu, J.; Li, L.; Lin, H.; Zhang, P.; Zhou, W.; Ma, Z. *Opt. Mater. Express* **2013**, *3*, 1313.
(20) Keiser, G. R.; Fan, K.; Zhang, X.; Averitt, R. D. *J. Infrared, Millimeter, Terahertz Waves* **2013**, *34*, 709−723.
(21) Engel, J.; Chen, J.; Liu, C. *Appl. Phys. Lett.* **2006**, *89*, 221907.
(22) Shir, D.; Ballard, Z. S.; Ozcan, A. *IEEE J. Sel. Top. Quantum Electron.* **2016**, *22*, 12−20.
(23) Xu, X.; Peng, B.; Li, D.; Zhang, J.; Wong, L. M.; Zhang, Q.; Wang, S.; Xiong, Q. *Nano Lett.* **2011**, *11*, 3232−3238. PMID: 21696183.
(24) Yang, A.; Hryn, A. J.; Bourgeois, M. R.; Lee, W.-K.; Hu, J.; Schatz, G. C.; Odom, T. W. *Proc. Natl. Acad. Sci. U. S. A.* **2016**, *113*, 14201−14206.
(25) Deubel, M.; von Freymann, G.; Wegener, M.; Pereira, S.; Busch, K.; Soukoulis, C. M. *Nat. Mater.* **2004**, *3*, 444−447.
(26) Meza, L. R.; Das, S.; Greer, J. R. *Science* **2014**, *345*, 1322−1326.
(27) Imboden, M.; Han, H.; Chang, J.; Pardo, F.; Bolle, C. A.; Lowell, E.; Bishop, D. J. *Nano Lett.* **2013**, *13*, 3379−3384.
(28) Imboden, M.; Han, H.; Stark, T.; Lowell, E.; Chang, J.; Pardo, F.; Bolle, C.; del Corro, P. G.; Bishop, D. J. *Nanoscale* **2014**, *6*, 5049−5062.
(29) Cowen, A.; Hardy, B.; Mahadevan, R.; Wilcensk, A. PolyMUMPs Design Handbook, 2013. http://www.memscap.com/__data/assets/pdf_file/0019/1729/PolyMUMPs-DR-13-0.pdf.
(30) Gissibl, T.; Wagner, S.; Sykora, J.; Schmid, M.; Giessen, H. *Opt. Mater. Express* **2017**, *7*, 2293.
(31) Jayne, R. K.; Stark, T. J.; Reeves, J. B.; Bishop, D. J.; White, A. E. *Adv. Mater. Technol.* **2018**, *3*, 1700293.

DOI: 10.1021/acs.nanolett.7b05042
Nano Lett. XXXX, XXX, XXX−XXX